

Dynamical history of a binary cluster: Abell 3653

Turgay Caglar¹ and Murat Hudaverdi^{1,2*}

¹*Yildiz Technical University, Faculty of Science and Art, Department of Physics, Istanbul 34220, Turkey*

²*AUM, College of Engineering and Technology, Department of Science, Dasman 15453, Kuwait*

Accepted 2017 August 10. Received 2017 August 10; in original form 2017 January 13

ABSTRACT

We study the dynamical structure of a bimodal galaxy cluster Abell 3653 at $z=0.1089$ by using combined optical and X-ray data. Observations include archival data from Anglo-Australian Telescope and X-ray observatories of XMM-Newton and Chandra. We draw a global picture for A3653 using galaxy density, X-ray luminosity and temperature maps. Galaxy distribution has a regular morphological shape at the 3 Mpc size. Galaxy density map shows an elongation EW direction, which perfectly aligns with the extended diffuse X-ray emission. We detect two dominant grouping around two brightest cluster galaxies (BCGs). The BCG1 ($z=0.1099$) can be associated with the main cluster A3653E, and a foreground subcluster A3563W concentrated at the BCG2 ($z=0.1075$). Both X-ray peaks are dislocated from BCGs by (~ 35 kpc), which suggest an ongoing merger process. We measure the subclusters' gas temperatures 4.67 and 3.66 keV, respectively. Two-body dynamical analysis shows that A3653E & A3653W are very likely (93.5% probability) gravitationally bound. The highly favoured scenario suggests that two subclusters with the mass ratio of 1.4 are colliding close to the plane of sky ($\alpha=17^\circ.61$) with 2400 km s^{-1} , and will undergo core passage in 380 Myr. Temperature map also significantly shows a shock-heated gas (6.16 keV) in between the subclusters, which confirms the supersonic infalling scenario.

Key words: X-rays – galaxies – clusters – individual: Abell 3653

1 INTRODUCTION

Cosmological models predict that small structures form first then progressively merge into larger structures. Clusters of galaxies are the largest gravitational entities of the Universe and their formation occurs at early epochs ($z \gtrsim 1$). Observations of forming clusters at high redshifts require long exposures and involve crucial technical difficulties. Nearby systems can still provide critical information about the structural formation; however, the evolutionary effects should be considered cautiously.

The dynamical consequence of a cluster merger is the transfer of energy ($\gtrsim 10^{64} \text{ ergs s}^{-1}$) and angular momentum of the merging subclusters to the system. Collisional nature of hot plasma and non-collisional nature of galaxies result in different reaction time scales during a merger (e.g., White & Fabian 1995; Roettiger et al. 1997). In such merging conditions extended ICM is strongly effected while individual galaxies can pass through. Brightest Cluster Galaxy (BCG) is defined as brightest galaxy in the cluster. BCGs are generally elliptical and are expected to be sitting at the bottom of the potential well of the parent cluster (e.g., Quintana & Lawrie 1982; Adami et al. 1998; Adami & Ulmer 2000). The

merger of BCG hosting clusters creates velocity offsets and dislocates BCG from the dynamical centre. Several observations have identified displaced BCGs from the cluster centre (e.g., Smith et al. 2005; Shan et al. 2010) and the number of BCGs with significant velocity gradient from the cluster mean (see e.g., Beers et al. 1991). Velocity comparison can measure the system's deviation from a relaxed configuration. Density maps which are produced by position and velocity information of cluster member galaxies, also reveal the footprints of substructures (e.g., Quintana et al. 1996; Berrena et al. 2009; Shakouri et al. 2016).

With the recent improvements on high angular resolution cameras, X-ray observations have played a key role to investigate merging clusters. The fate of the merger energy and the complexity of collisional ICM have been considerably settled. Apparently, kinetic energy of the merging structures is converted into thermal energy of the plasma, which has been observed in many clusters (e.g., Markevitch & Vikhlinin 2007; Bourdin & Mazzotta 2008).

In this paper, we present the structural analysis results of Abell 3653 (A3653 hereafter). The cluster's BCG is known to have one of the most extreme radial velocities (Pimblet et al. 2006), which is a strong suggestion for a recent or ongoing merger activity. The original optical data were studied for signs of substructure by Pimblet et al. (2006), but they

* E-mail: hudaverd@yildiz.edu.tr (MH)

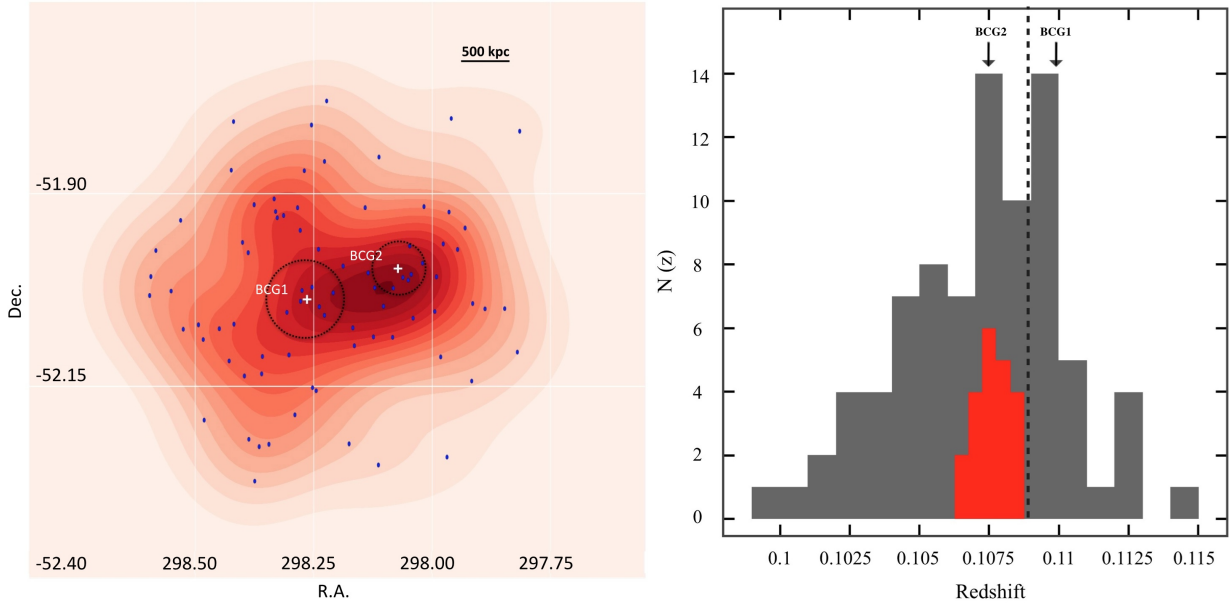


Figure 1. Left: Galaxy density map A3653 within 1.5 Mpc radius field. The white crosses indicate the BCG positions. Right: Redshift histogram of A3653 for 84 member galaxies. The vertical dotted line gives the mean cluster value, and two arrows are the redshifts of the BCGs. The red histogram shows the member galaxies around the BCG2 ($0.10625 < z < 0.10875$).

did not report any significant grouping. A3653 was also studied in the *MCMX* meta-catalogue based on *ROSAT* All Sky Survey (Piffaretti et al. 2011). The *MCMX* provides a redshift of 0.1069, a standardized 0.1–2.4 keV band luminosity $L_{500} = 1.57 \times 10^{44}$ ergs s^{-1} , total mass of $M_{500} = 2.5 \times 10^{14} M_{\odot}$, and radius of $R_{500} = 925.8$ kpc. In order to understand the dynamical structure of A3653, we investigate X-ray morphology and temperature distribution with archival *XMM-Newton* and *Chandra* observations. Raw X-ray image shows a clear bimodal structure with X-ray centroids: A3653E (J2000, RA:19^h53^m01.9^s, DEC.:−52^d02^m13^s), and A3653W (J2000, RA: 19^h52^m17.3^s, DEC.:−51^d59^m50^s) (see Figure-2).

In this study, we aim to describe X-ray morphology and temperature structure of Abell 3653. Besides, we focus on explaining A3653 physical mechanism occurred with dynamical merge activities. We compare our X-ray results with optical results studied by Pimblet et al. (2006). The optical study signs that A3653 has 111 galaxies at cluster field. A3653 is located at RA= 19^h53^m00.9^s and Dec.: −52^d01^m51^s with redshift (z) value of 0.1089 (Struble & Rood 1999). In addition, A3653 is a rich centrally condensed cluster (Gregorini et al. 1994).

This paper is organised as follows; in Section 2, we describe the data used in our analysis. In Section 3, the analysis of the X-ray and optical observations is described, the temperature distribution is studied in detail. In Section 4, we discuss cluster dynamics and possible subclusters. We summarise our results in Section 5. We adopt cosmological parameters $H_0 = 70$ km s^{-1} Mpc $^{-1}$, $\Omega_M=0.27$ and $\Omega_{\Lambda}=0.73$ in a flat universe. For this cosmology, an angular size of 1 arcmin corresponds to a physical scale of 119.22 kpc at the redshift of A3653 ($z=0.1089$). Unless otherwise stated, reported errors correspond to 90% confidence intervals.

2 OBSERVATIONS AND DATA REDUCTION

2.1 Optical Spectroscopic Data

We obtained galaxy spectroscopic redshifts using Anglo-Australian Telescope (*AAT*). In the literature, there are several velocity measurement studies performed for a variety of samples. We selected galaxies within a 3.0 Mpc radius of the A3653 centroid with a spectroscopic redshift falling in the interval $0.099 < z_{spec} < 0.115$, which fairly captures the range of galaxies associated with A3653. Our selection includes total 87 members; 83 galaxies from 2dF (Pimblet et al. 2006) and 4 galaxies from 6dF Galaxy Survey final redshift release (Jones D. H. et al. 2009). The member galaxies are listed in the appendix.

Projected galaxy density map of member galaxies is shown in Figure-1 left-panel. Galaxies identified as cluster members from spectroscopy are marked with dots. Two plus signs are the locations of the BCGs. Two circles are superimposed for visual aid, shows the extended X-ray count extraction regions used for the spectral analysis in the following sections. The galaxy density distribution shows an elongated structure East-West axis with a little tilt.

On the basis of 87 redshifts, we plot a redshift histogram of A3653 (see Figure 1 right-panel). The vertical dotted line shows the mean cluster redshift value of $z = 0.1089$. The cluster’s BCG is known as having one of the most extreme radial velocity $\sigma_{cz} = 683 \pm 96$ km s^{-1} away from the mean cluster velocity (Pimblet et al. 2006), which locates it considerably further at $z = 0.1099$. Although a gaussianity is visible around the cluster mean $z = 0.1089$, deviations from a single Gaussian can be attributed to the subclusters around two BCGs. The BCG1 at $z = 0.1099$ can be associated with the main cluster, and a foreground west clump concentrated around the galaxy 2MASX J19521735-5159465 at $z=0.1075$ (Jones D. H. et al. 2009). The galaxy is catalogued with $(r_F, b_J) = (15.20, 16.11)$

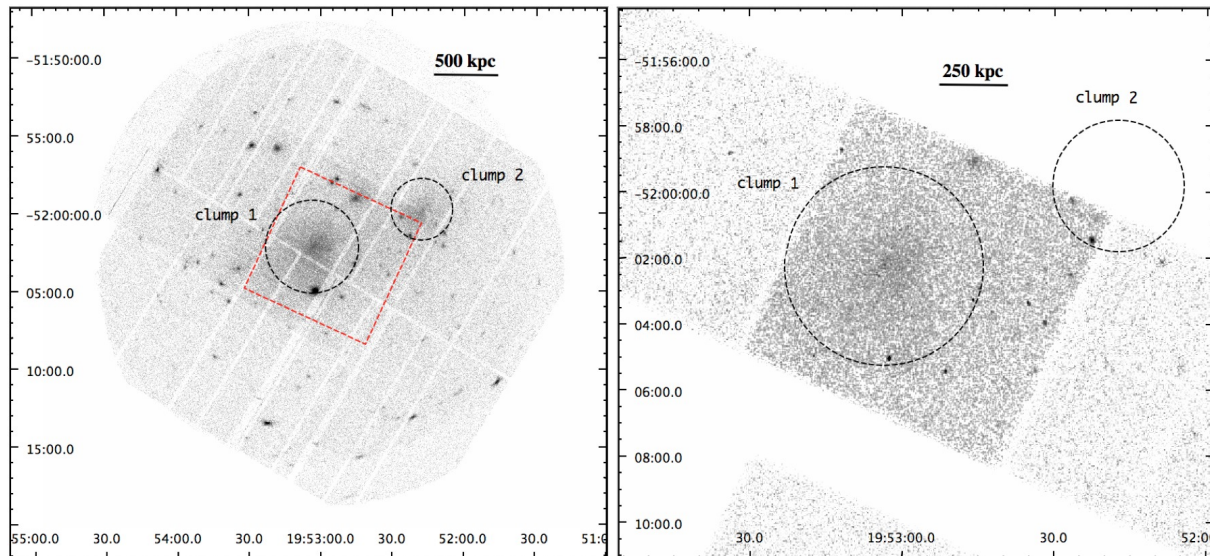


Figure 2. The panels are the *XMM-Newton* mosaic image of MOSs/PN in the 0.3–10 keV (left) and the *Chandra* ACIS-S3 in the 0.5–7 keV (right) energy ranges, background and exposure corrected images. The subclusters are circled with the circles used for the spectral extraction. The tilted square region on the *XMM-Newton* image corresponds *Chandra* FOV. The images are adaptively smoothed in order to highlight the structures with extended plasma emission.

Table 1. Log of X-ray Observations.

ObsID	Satellite	Date Obs	Effective Exposure Time (ks)
10460	<i>Chandra</i>	2009-07-05	ACIS 43.6 (%98.6)
0691820101	<i>XMM-Newton</i>	2013-03-18	MOS1 48.6 (%75.2) MOS2 48.8 (%75.5) PN 47.5 (%78.3)

magnitudes in the NASA Extragalactic Database (NED). Considering its location at the X-ray centroid of A3653W and being two magnitude brighter than neighboring members, 2MASX J19521735-5159465 is named as BCG2 hereafter. The BCG2 was unexpectedly not included in the 2dF galaxy survey study of Pimbblet et al. (2006). This is possibly the reason why the cD galaxy of A3653 and its peculiar velocity could not be explained with no significant grouping. The redshift values of the two BCGs are indicated in the histogram Figure-1 right-panel. Since we are interested in the potential subgroups associated with merging scenarios, we also identify the galaxies clustering around BCG2 with $V_r = 32221 \pm 350 \text{ km s}^{-1}$ interval ($0.10625 < z < 0.10875$) displayed in Figure 1 (red colour). Their spatial properties are discussed with X-ray analysis results in later sections, consecutively.

2.2 X-Ray Observations

We used *XMM-Newton* and *Chandra* archival data for our analysis (see Table-1). *XMM-Newton* observation was performed March 19, 2013 for an exposure time of 64 ks with observation id 0691820101. The MOS and PN detectors in Full Frame Mode and Extended Full Frame respectively, with

the thin filter. Observation data was obtained from *XMM-Newton* Science Archive. We performed the data processing and background modeling with the *XMM* Extended Source Analysis Software (*XMM-ESAS*: Snowden et al. (2008)) and *XMM-Newton* Scientific Analysis System (*XMMSAS*) v14.0. The event files for MOSs and pn were created using *emchain* and *epchain*, respectively. We filtered bad pixels, bad columns and cosmic rays using *evselect*. The total filtered MOS1, MOS2 and pn exposure times are 48.6 ks, 48.8 ks and 47.5 ks, respectively.

The *Chandra* observation of A3653 was carried out on 2009 July 5 (Obs ID 10460) for a total exposure of 44.2 ks with CCDs 3, 5, 6, 7, and 8 of Advanced CCD Imaging Spectrometer (ACIS) in operation, telemetered in the VFAINT mode. We obtained observation data from *Chandra* Data Archive. Most of the X-ray emissions of A3653 are covered by the ACIS-S3 chip. Therefore, this study focuses on the S3 chip. The data were reprocessed from level 1 event files using CIAO 4.8 and CALDB 4.7.0. The total altered ACIS exposure time is 43.6 ks.

3 ANALYSIS

We generated broad-band images from *XMM-Newton* in the 0.3–10 keV and *Chandra* in the 0.5–7 keV, respectively. Figure 2 shows adaptively smoothed images without exposure and background correction. The left-panel is *XMM-Newton* mosaic image MOSs/PN. Exposure corrected *Chandra* image of extended diffuse emission for A3653 is created by using *fluximage* (Fig. 2 right-panel). *XMM-Newton* observation covers almost entire cluster emission, while narrow *Chandra* field-of-view (FOV) of ACIS-S3 only collects photons from the main cluster. The tilted square at the *XMM-Newton* image displays ACIS-S3 FOV, and the two circles are selected X-ray emission regions for global spectral anal-

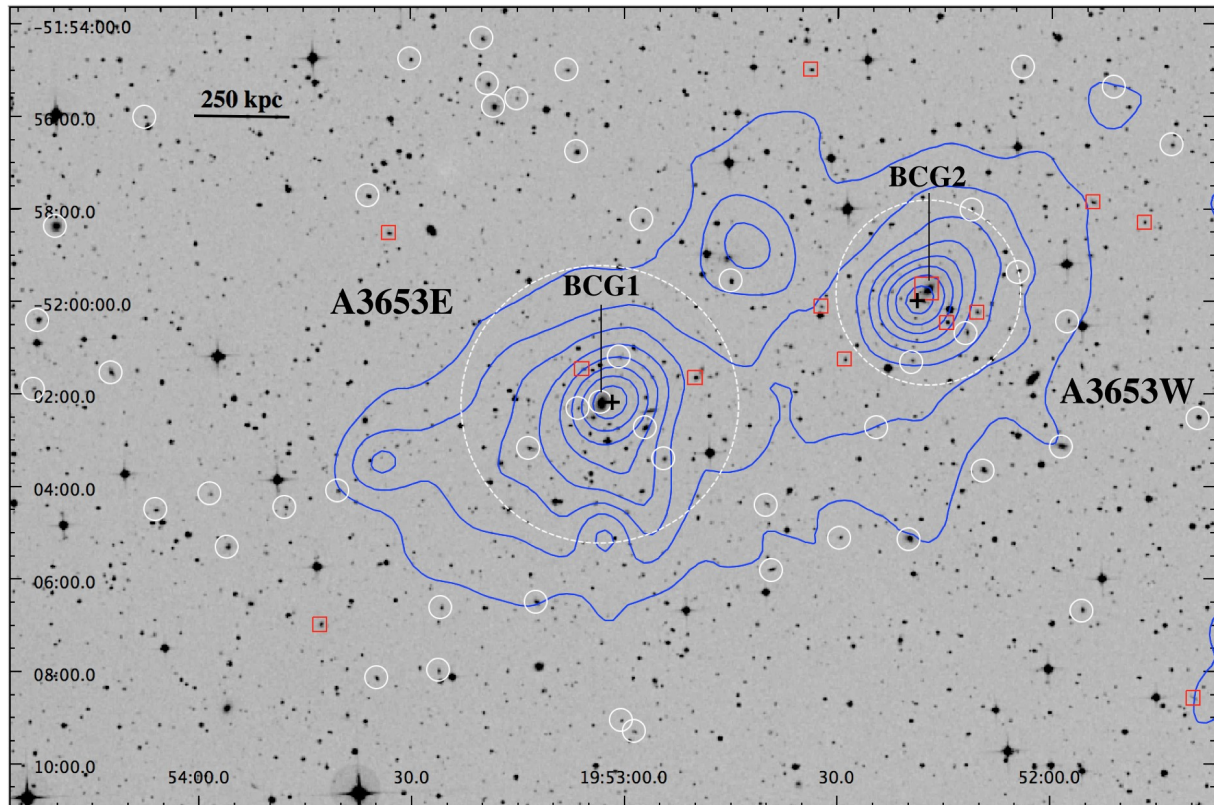


Figure 3. Contours of the X-ray diffuse emission at 0.3 – 10 keV from MOS logarithmically spaced by a factor of 0.7 and overlaid on the DSS optical image. The subclusters are indicated with dashed circles. The positions of the subcluster X-ray peaks are indicated by plus signs, and associated BCGs are pointed by arrows. The galaxies identified as cluster members are marked with the white circles. The red boxes indicate the galaxies with $V_r = 32221 \pm 350 \text{ km s}^{-1}$ interval around BCG2.

ysis. The subclusters do not have bright central cores or regular morphologies, as is typical of non-cool core clusters.

The locations of the point sources in the FOV are detected using `edetect_chain` in the 0.2 – 12 keV energy band for *XMM-Newton*. For *Chandra* data, we used CIAO’s `wavdetect` in the 0.5 – 8 keV energy band. We have all point sources at 4σ confidence level excluded by masking the event files and thereby decreasing the contribution of point sources to the extend ICM emission.

Figure 3 shows the contours from the combined MOS images in the 0.3 – 10 keV energy band, overlaid on the DSS optical image for A3653. Since the PN image is disrupted by chip gaps at the central regions (see Fig. 2), we rejected PN data for imaging and the related analysis. The X-ray image was adaptively smoothed and corrected for the background, exposure time, and vignetting. Two regions used for the spectral extraction for the subcluster extend emission are indicated with dashed circles. The positions of the subcluster X-ray peaks (A3653E & A3653W) are indicated by plus signs. BCG1 and BCG2 are pointed by arrows to underline their evident relations with A3653E and A3653W, respectively. However the X-ray peaks does not exactly match with the BCGs, there is a clear shift $\sim 35 \text{ kpc}$ for both. These type of positional disturbances can be associated with an ongoing merger activity, which may dislocate BCGs from the dynamical centre. The cluster member galaxies from spectroscopy are marked with circles. The red boxes are the members of the sub-sample, which has redshift values clustering at

A3653W redshift ($z = 0.1075 \pm 0.0012$). At this redshift range there are 21 members but spatially dispersed, which is not straightforward to determine an optical subcluster.

3.1 Spectral Analysis

We examined the spectra of each subcluster to determine the global properties of the ICM. The spectrum of A3653E is extracted and studied for *XMM-Newton* and *Chandra* since it is clearly viewed from both cameras. The western sub-cluster A3653W is analysed only by *XMM-Newton* for lack of *Chandra* observation in that region. *XMM-Newton* spectra and response files were generated using `evselect` V3.6.2, `rmfgen` V2.2.1 and `arfgen` V1.90.4. An annular region $11' - 12'$ away from the cluster centroid is used to extract the local background. To model the background, we used the CALDB blank sky event files for *Chandra*. The spectral files are generated by using `specextract`. The spectra from the observations were fitted using the XSPEC software package, version 12.9.0. (Arnaud 1996). Temperature and abundance were allowed to be free parameters. We adopt the solar abundance table from Anders & Grevesse (1989). Varying the galactic absorption column density did not significantly influence the primary parameters or improve the spectral fits. Therefore in all cases, the value is fixed at A3653 position on the sky from the Leiden/Argentine/Bonn (LAB) Survey (Kalberla et al. 2005) of $N_H = 4.14 \times 10^{20} \text{ cm}^{-2}$.

For *XMM-Newton* data, the energies outside the range

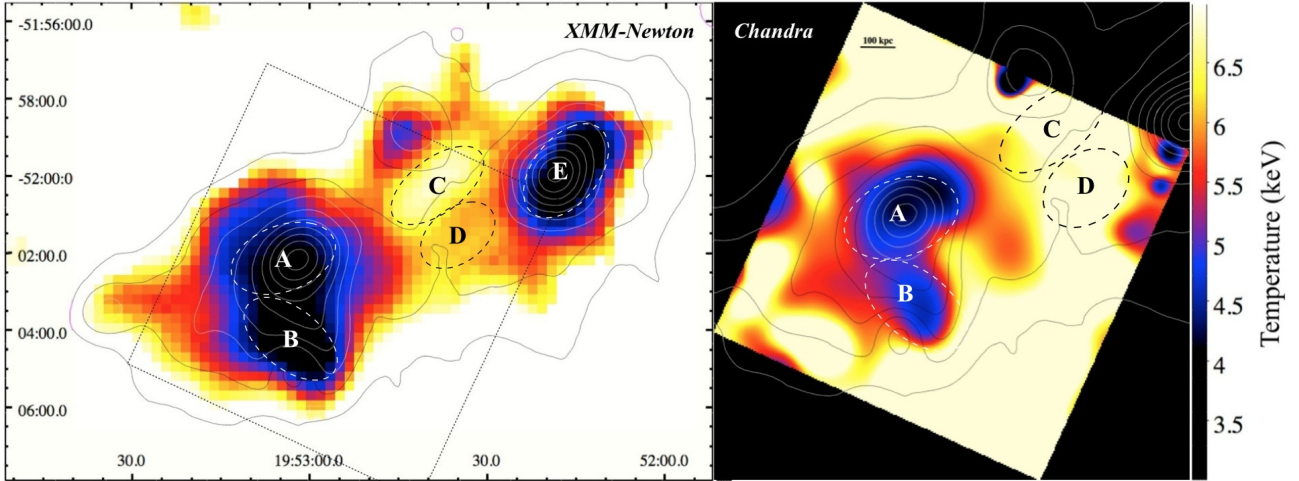


Figure 4. Temperature map obtained by hardness ratio approximation method for *XMM-Newton* (left) and *Chandra* (right) (see §3.2 for detail). The color-coding ranges are from black (~ 4 keV) to yellow (>6 keV). X-ray contours (as in Fig.3) are superimposed for visual aid. The tilted-square shows *Chandra* FOV. The regions used for the spectroscopic analysis are displayed in ellipses.

Table 2. The best-fit parameters of spectral modeling for A3653 subclusters with ¹*XMM-Newton* and ²*Chandra* data.

Region	kT (keV)	Abundance (Z_{\odot})	χ^2/dof
A3653E ¹	4.67 ± 0.20	0.15 ± 0.05	$2162/1760 = 1.23$
A3653E ²	4.67 ± 0.46	$0.24^{+0.14}_{-0.13}$	$289/251 = 1.15$
A3653W ¹	$3.66^{+0.29}_{-0.28}$	$0.27^{+0.09}_{-0.08}$	$1241/1223 = 1.01$

0.3 – 10 keV were ignored. The EPIC-MOS and PN spectra were fitted simultaneously, after checking the consistency. The bright instrumental lines due to quiescent particle background (QDP); Al-K α (1.49 keV), Si-K α (1.74 keV) for MOS and Al-K α , Cu-K α (8.05, 8.91 keV) for PN are carefully ignored from spectral data. The *Chandra* fitting was performed in the 0.5 – 7 keV energy range. The blank sky event files normalised at 10 – 12 keV band to the count rate of the observation to account for the QDP. We used an absorbed single temperature collisional equilibrium plasma (APEC) model. For A3653E subcluster, the model gives a temperature of $kT = 4.67 \pm 0.20$ keV and an abundance of $Z = 0.14 \pm 0.05 Z_{\odot}$ for *XMM-Newton*. For the same region, the best-fit parameters of *Chandra* data are highly consistent within the error range; the temperature is $kT = 4.67 \pm 0.46$ keV, and the abundance is $Z = 0.20^{+0.14}_{-0.13} Z_{\odot}$. Since we lacked *Chandra* observation, the spectral modeling is only performed for *XMM-Newton* data for western subcluster A3653W. The best fit parameters for the spectral modelling within 2.5 arcmin radius circle are $3.66^{+0.29}_{-0.28}$ keV of temperature and $0.27^{+0.09}_{-0.08} Z_{\odot}$ of abundance. The results from the spectral fitting are summarised in Table 2.

3.2 Temperature Map

Temperature maps are very powerful tools and provide useful information about temperature discontinuities due to the ongoing merger. To search for evidence, we generated a temperature map for A3653 with hardness ratio approximation.

Table 3. Comparison of the temperature map (T_{map}) values with spectroscopically derived temperatures (T_{spec}).

Region	T_{map} (keV)	T_{spec} (keV)	χ^2/dof
A	4.21 ± 0.49	$4.30^{+0.34}_{-0.28}$	$1166/1122 = 1.03$
B	3.66 ± 0.63	$3.78^{+0.36}_{-0.35}$	$717/693 = 1.03$
C	6.08 ± 0.99	$6.16^{+1.40}_{-1.20}$	$373/364 = 1.02$
D	5.98 ± 0.97	$6.06^{+1.20}_{-1.10}$	$575/485 = 1.18$
E	3.65 ± 0.57	$3.38^{+0.49}_{-0.53}$	$240/241 = 1.00$

The images have been extracted in soft and hard energy bands carefully by avoiding QDP instrumental lines, galactic absorption at soft bands (< 0.7 keV) and point source emissions at hard bands (> 8 keV). Point sources excluded event files used for the analysis, but the source excluded holes were filled using the surface brightness of the surrounding pixels and the CIAO tool `dmfilt`. The soft and hard energy bands were selected to have approximately equal photon counts, which is also statistically favourable. The hardness ratio maps are produced by the images at energy bands 0.8 – 1.6 keV and 1.8 – 8 keV from *XMM-Newton* MOSs, 0.7 – 1.6 keV and 1.6 – 7 keV for *Chandra* ACIS-S3 counts, respectively. The hard images are divided by the corresponding soft images to obtain a hardness ratio map. The pixel ratio values of the map are converted to temperature values by multiplying the theoretical conversion factors. The factors are determined using an absorbed single thermal collisional plasma model (wabs + APEC), with a column density fixed to the Galactic value of $N_H = 4.14 \times 10^{20} \text{ cm}^{-2}$, and the redshift at $z = 0.1089$. A similar technique for producing temperature map from hardness ratio is outlined in Ferrari et al. (2006).

Figure 4 shows the temperature map obtained through the hardness ratio technique for *XMM-Newton* (left) and *Chandra* (right). The color-coding is arranged to display the similar temperature values for both, which range from black (~ 4 keV) to yellow (~ 6 keV). The *Chandra* and *XMM-*

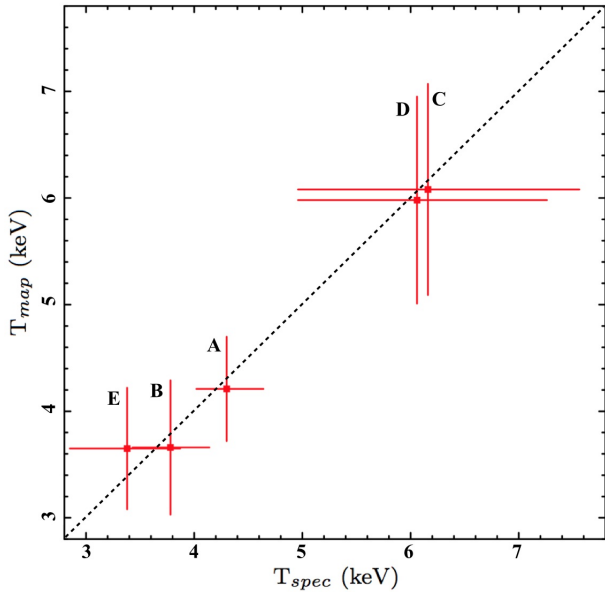


Figure 5. The plot of the T_{spec} vs. T_{map} for 5 peculiar regions. The ratios vary around 1 (inclined line), which confirms consistency and the agreement of the values.

Newton temperature structure and the variation display similar properties within the common frame, which is shown with a square in the left panel. Based on the temperature map, A3653 is characterized by two cold (~ 3.5 to 4.5 keV) regions associated with A3653E & A3653W, and a hot (~ 6 keV) region in between.

The confidence of the produced temperature map is spectroscopically confirmed with 5 control regions (labelled A, B, C, D and E) as shown in Figure 4. The spectroscopic temperature values (T_{spec}) are estimated from *XMM-Newton* MOSs/PN simultaneous fit with N_H fixed to the galactic value, and provide a reduced $\chi^2 \simeq 1$. Table 3 compares these best-fit temperature values (T_{spec}) with the values obtained directly from temperature maps (T_{map}). The values are in good agreement within the error range. Figure 5 shows the plot of T_{spec} vs. T_{map} values and visually confirms the consistency. The ratio values neatly vary around 1 (inclined-line), where T_{spec} and T_{map} are equal.

Temperature map study and related spectral analysis results verify that A3653E (4.67 KeV) and A3653W (3.66 keV) has relatively cool cores. There is a significantly hot (6.16 keV) distinct region between the subclusters. If we assume that the subclusters are gravitationally bound and moving towards each other, the hot region seems like shock heated by a possible merger event.

4 MASS ANALYSIS

The mass of isothermal clusters is estimated to scale with the X-ray emission-weighted temperature by $M \propto T_x^{3/2}$ as predicted by simulations (e.g., Eke et al. 1996) and observations (e.g., Markevitch 1998). A similar assumption gives us a mass ratio of 1.4:1.

The masses were also quantitatively estimated using the $M - T$ relation derived without groups by Finoguenov et al.

Table 4. Properties of A3653 system.

Parameter	A3653E	A3653W
z	0.1099 ± 0.0002^a	0.1075 ± 0.0002^b
V_r (km s $^{-1}$)	32947 ± 66^a	32221 ± 45^b
$M(M_\odot)$	4.06×10^{14}	2.77×10^{14}

^aPimblet et al. (2006), ^bJones D. H. et al. (2009)

(2001):

$$M_{500} = (3.57_{-0.35}^{+0.41}) 10^{13} \times kT_{ew}^{1.58_{-0.07}^{+0.06}} \quad (1)$$

A3653E has a best-fit global temperature of 4.67 ± 0.20 keV, and an abundance of $0.15 \pm 0.05 Z_\odot$ value. The scaling relation estimates a total mass of $4.06 \times 10^{14} M_\odot$ for A3653E subcluster. The best fit temperature of A3653W is $3.66_{-0.28}^{+0.29}$ keV, with an abundance of $0.27_{-0.08}^{+0.09} Z_\odot$. The scaling relation predicts a total mass of $2.77 \times 10^{14} M_\odot$ for A3653W. These numeric mass estimations also give a mass fraction of ~ 1.4 , consistently. Table 4 lists redshifts, the relative velocity of BCGs and total masses of A3653 subclusters.

5 A DYNAMICAL MODEL FOR A3653E & A3653W

We apply the Newtonian gravitational binding criterion that two-body system is bound if the potential energy of the system is equal or greater than the kinetic energy. The two-body dynamical model was described in detail by Beers et al. (1982) and Gregory & Thomson (1984). The model was also successfully applied to several bimodal systems in the literature: e.g. A1367 (Cortese et al. 2004), A168 (Hwang & Lee 2009), A2319 (Yan et al. 2014), A3716 (Andrade-Santos et al. 2015), A3407 & A3408 (Nascimento et al. 2016) and A1750 (Hwang & Lee 2009; Bulbul et al. 2016). This model allows us to evaluate the dynamical state of A3653E and A3653W and to estimate the probability that (i) the system infalling, (ii) the system is gravitationally bound but still expanding, or (iii) the subclusters are unbound but are projectionally close together in the sky by chance. The limits of the bound solutions for a system can be determined by using the Newtonian criterion for gravitational binding (Beers et al. 1982):

$$V_r^2 R_p \leq 2GM \sin^2 \alpha \cos \alpha \quad (2)$$

The radial velocity difference, V_r , and the projected separation, R_p , are related to the real velocity and separation of the system parameters by

$$V_r = V \sin \alpha, \quad R_p = R \cos \alpha. \quad (3)$$

The angle α is the projection angle between the plane of the sky and the line connecting the subsystems (i.e., $\alpha=0$ if the subclusters are at the same distance). V and R are true (3D) velocity and positional separation between the two subclusters. For the gravitationally bound systems the parametric solutions to the equation of motion (Beers et al. 1982) :

$$t = \left(\frac{R_m^3}{8GM} \right)^{1/2} (\chi - \sin \chi), \quad (4)$$

$$R = \frac{R_m}{2}(1 - \cos \chi), \quad (5)$$

$$V = \left(\frac{2GM}{R_m} \right)^{1/2} \frac{\sin \chi}{(1 - \cos \chi)}, \quad (6)$$

where R is the separation at time t , R_m is the separation at the maximum expansion, M is the combined mass of the system, and χ is the developmental angle. Similarly, the parametric solutions for the unbound case is also described by Beers et al. (1982). For gravitationally unbound systems, the parametric equations are

$$t = \frac{GM}{V_\infty^3}(\sinh \chi - \chi), \quad (7)$$

$$R = \frac{GM}{V_\infty^2}(\cosh \chi - 1), \quad (8)$$

$$V = V_\infty \frac{\sinh \chi}{(\cosh \chi - 1)}, \quad (9)$$

where V_∞ is the asymptotic expansion velocity. Using the parameters previously found for A3653 subclusters: radial velocity difference of $V_r = 726 \pm 80 \text{ km s}^{-1}$, the projected distance (R_p) on the plane of the sky between the X-ray centers of the subclusters as 0.89 Mpc, total mass of $M = 6.83 \times 10^{14}$ (see Table 4), and setting $t = 12.1 \text{ Gyr}$ ($3.8 \times 10^{17} \text{ s}$) the age of the universe at A3653 redshift, we can constrain the equations. Subsequently, the radial velocity difference (V_r) as a function of the projection angle (α) between the subclusters are solved by equation (6) of Gregory & Thomson (1984) for bound and unbound states are

$$\tan \alpha = \frac{tV_r}{R_p} \frac{(\cos \chi - 1)^2}{\sin \chi (\chi - \sin \chi)}, \quad (10)$$

$$\tan \alpha = \frac{tV_r}{R_p} \frac{(\cosh \chi - 1)^2}{\sinh \chi (\sinh \chi - \chi)}, \quad (11)$$

respectively.

The solution for A3653 system is shown in Figure 6. The projected angle (α) as a function of the radial velocity difference (V_r) is plotted for bound (red line) and unbound (blue line) solutions. The black curve separates the bound and unbound regions according to the Newtonian criterion. Since the relative radial velocity of our system is observed to be $V_r = 726 \pm 80 \text{ km s}^{-1}$, we obtain two bound solutions and one unbound solution. All three solutions (black circles in Fig-6) are defined by the intersections of curved lines with the solid vertical line corresponding the relative velocity difference ($V_r = 726 \pm 80 \text{ km s}^{-1}$) between the two clusters in the rest frame of A3653. The uncertainties in the measured velocity lead to a range of solutions from α_{inf} to α_{sup} for the projection angles. We compute relative probabilities for the solutions by the formula (Girardi et al. 2005):

$$p_i = \int_{\alpha_{inf,i}}^{\alpha_{sup,i}} \cos \alpha \, d\alpha \quad (12)$$

where each solution is represented by index i . The probabilities are normalised by $P_i = p_i / (\sum_i p_i)$.

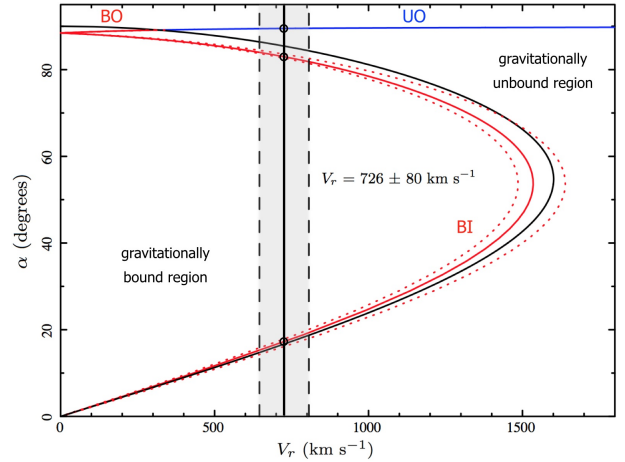


Figure 6. Projection angle (α) as a function of the relative radial velocity difference (V_r) of the subclusters A3653E and A3653W. BI, BO and UO stand for Bound-Incoming, Bound-Outgoing, and Unbound-Outgoing solutions. Red and blue lines correspond to bound and unbound solutions, respectively. The black curve separates the bound and unbound regions according to the Newtonian criterion. The vertical lines represent the relative radial velocity, $V_r = 726 \pm 80 \text{ km s}^{-1}$, between the two clusters in the rest frame of A3653. The black circles are the three acceptable solutions.

Solving the parametric equations we get two gravitationally bound incoming solutions and one unbound outgoing solution. For the bound solutions, the subclusters are either approaching to each other at 732 km s^{-1} (6.5% probability) or at 2400 km s^{-1} (93.5% probability). The first solution suggest that subcluster cores will cross each other after a long time (9.7 Gyr) given a separation of 7.24 Mpc with a mean colliding velocity of 732 km s^{-1} . This bound scenario apparently does not predict a strong interaction between A3653E and A3653W, thus the solution has a low probability (6.5%). The latter more likely scenario corresponds to a collision in about 380 Myr, considering their separation of 0.93 Mpc with a supersonic colliding velocity of 2400 km s^{-1} . Temperature map (Fig-5) also confirms a hot region and spectral fit gives $kT = 6.16_{-1.20}^{+1.40} \text{ keV}$, providing evidence of shock heated gas between the subclusters. The large angle ($\alpha = 89^\circ.49$) unbound solution (0.05% probability) corresponds to a separation of 71.3 Mpc. The parameters of these solutions are presented in Tables 5 and 6. Given its negligibly low probability, the unbound solution can be disregarded, while the bound solution close to the plane of sky ($\alpha = 17^\circ.61$) is highly favoured (93.5% probability).

The dynamical model analysis result for A3653 is fairly conclusive that the subclusters are very likely gravitationally bound, and the cores will cross each other in 380 Myr. Normally, approaching systems produce strong ram pressure and displace X-ray plasma (Vijayaraghavan & Ricker 2013). In our case, X-ray peaks are found to be in the opposite direction. This suggests that it is not the first encounter of the subclusters; therefore, there was a previous core passage. The probabilities for the bound solutions should be treated cautiously, since the dynamical two-body model assumes a clear radial infall (e.g. head-on merger) and does not include the angular momentum information of the subclusters, which is very unlikely to be zero. If the merging between the subclusters occurs with angular momentum as

Table 5. Best-Fit Parameters for the Bound Incoming Solutions of the Dynamical Model. The columns list best-fit values for χ and α for the bound solutions, and the corresponding values for R , R_m , V and the related probabilities P .

χ (rad)	α (degrees)	R (Mpc)	R_m (Mpc)	V (km s ⁻¹)	P (%)
5.05	82.94	7.24	21.50	731.5	6.5
5.86	17.61	0.93	20.88	2399.7	93.5

Table 6. Best-Fit Parameters for the Unbound Outgoing Solutions of the Dynamical Model. The columns list best-fit values for χ and α for the bound solutions, and the corresponding values for R , V , V_∞ and the related probabilities P .

χ (rad)	α (degrees)	R (Mpc)	V (km s ⁻¹)	V_∞ (km s ⁻¹)	P (%)
3.16	89.49	71.30	726.03	666.88	0.02

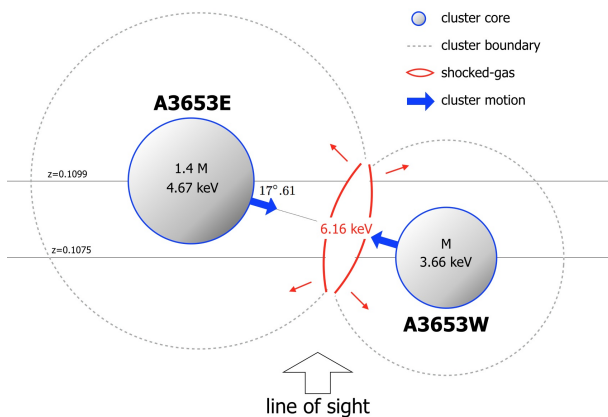


Figure 7. Tentative illustration of A3653E & A3653W subclusters gravitationally falling into each other (blue-arrows). The merger is happening very close to the plane of sky (horizontal-lines). The cluster boundaries (dotted-circles) start to collide and develop a shocked region (in red). The line of sight is depicted with big arrow at the bottom.

in off-axis mergers, consequences will be more complicated as shown in the simulations (Takizawa 2000; Vijayaraghavan & Ricker 2013).

6 SUMMARY

We present the analysis results of a merging binary cluster A3653 using *AAT* Optical Galaxy Survey Data, *XMM-Newton* and *Chandra* X-ray observations. Spectroscopic redshift analysis, X-ray brightness & temperature maps and two-body dynamical model analysis clearly indicate that A3653 is not a single structure but composed of two subclusters. A possible interpretation of our findings is illustrated in Figure 7. Our main results are:

- On the basis of the optical spectroscopic redshifts of 87

member galaxies with *AAT* Galaxy Survey data, A3563 has a mean cluster redshift value of $z = 0.1089$. We detect two dominant grouping of member galaxies; BCG1 at $z=0.1099$, can be associated with the main cluster and a little foreground western subgroup concentrated at $z=0.1075$, BCG2 (see Fig-1).

- X-ray brightness map also clearly indicates the binary structure of A3653 with two distinct clumps (see Fig-2). The X-ray peaks match with BCGs by a small disturbance (~ 35 kpc), which is probably caused by ram-pressure of an ongoing dynamical activity (see Fig-3). The displacement of the peaks aligns with the elongation of the subcluster locations, which suggest that the peak shifts are associated with the merger activity. However, the position of the peaks imply that there was a previous core passage between the subclusters.

- Average temperature values of A3563E and A3563W are 4.67 keV and 3.66 keV, respectively. Based on the temperature map, we detect a possible shock heated gas with a significantly elevated temperature of $kT = 6.16$ keV between the two subclusters (see Fig-4). The hot gas results from shock heating by merging subclusters.

- The mass calculations for isothermal clusters result in $M_{A3653E} = 4.06 \times 10^{14} M_\odot$ and $M_{A3653W} = 2.77 \times 10^{14} M_\odot$. A3653 is composed of two merging subclusters with ~ 1.4 mass fraction.

- The two-body dynamical model suggests three solutions: two collapsing and one unbound expanding (see Fig-6). Based on the analysis, the unbound solution has negligibly low (0.02%) probability. The subclusters are gravitationally bound and infalling. The merging is happening close to the plane of sky ($\alpha=17^\circ.61$), and the cores will cross each other in 380 Myr.

ACKNOWLEDGEMENT

We would like to acknowledge financial support from the Scientific and Technological Research Council of Turkey (TÜBİTAK) project number 113F117. The work is also supported by YTU Scientific Research & Project Office (BAP) funding with contract numbers 2013-01-01-YL01 and 2013-01-01-KAP04. The authors would like to thank S. Alis for the useful discussion and suggestions.

REFERENCES

- Adami C., Mazure A., Katgert P., Biviano A., 1998, *A&A*, 336, 63
- Adami C., Ulmer M. P., 2000, *A&A*, 361, 13
- Anders E., Grevesse N., 1989, *GeCoA*, 53, 197
- Andrade-Santos F. et al., 2015, *ApJ*, 803, 108
- Arnaud K. A., 1996, 101, 17
- Beers T. C., Geller M. J., Huchra J. P., 1982, *ApJ*, 257, 23
- Beers T.C., Gebhardt K., Forman W., Huchra J.P., Jones C., 1991, *AJ* 102, 1581
- Barrena R., Girardi M., Boschin W., Dasi M., 2009, *A&A* 503, 357
- Bourdin H., Mazzotta P., 2008, *A&A*, 479, 307
- Bulbul E. et al., 2016, *APJ*, 818, 131
- Cortese L., Gavazzi G., Boselli A., Iglesias-Paramo J., Carrasco L., 2004, *A&A*, 425, 429
- Eke V. R., Cole S., Frenk C. S., 1996, *MNRAS*, 282, 263

- Ferrari C., Arnaud M., Ettori S., Maurogordato S., Rho J., 2006, *A&A*, 446, 417
- Finoguenov A., Reiprich T. H., Böhringer H., 2001, *A&A*, 368, 749
- Girardi M. et al., 2005, *A&A*, 436, 29
- Gregorini L., de Ruiter H. R., Parma P., Sadler E. M., Vettolani G., Ekers R. D., 1994, *A&A*, 106, 1
- Gregory S. A., Thompson L., 1984, *ApJ*, 286, 422
- Hwang H. S., Lee M. G., 2009, *MNRAS*, 397, 2111
- Jones D. H. et al., 2009, *MNRAS*, 399, 683
- Kalberla P. M. W. et al. 2005, *A&A*, 440, 775
- Markevitch M., 1998, *A&A*, 504, 27
- Markevitch M., Vikhlinin A., 2007, *Phys. Rep.*, 443, 1
- Nascimento R. S. et al., 2016, *MNRAS*, 460, 2193
- Yan P., Yuan Q., Zhang L., Zhou X., 2014, *APJ*, 147, 106
- Piffaretti R., Arnaud M., Pratt G. W., Pointecouteau E., Melin J. B., 2011, *A&A*, 534, A109
- Pimblett K. A., Roseboom I. G., Doyle M. T., 2006, *MNRAS*, 368, 651
- Quintana H., Lawrie D. G., 1982, *AJ*, 87, 1
- Quintana H., Melnick J., Proust D., Infante L., 1996, *A&AS*, 125, 247
- Roettiger K., Loken C., Burns J.O., 1997, *ApJS*, 109, 307
- Shakouri S., Johnston-Hollitt M., Dehghan S., 2016, *MNRAS*, 458, 3083
- Shan H., Qin B., Fort B., Tao C., Wu X., Zhao H., 2010, *MNRAS*, 406, 1134
- Smith G. P., Kneib J., Smail I., Mazzotta P., Ebeling H., Czoske O., 2005, *MNRAS*, 359, 417
- Snowden S.L., Mushotzky R.F., Kuntz K.D., Davis D.S., 2008, *A&A*, 478, 615
- Struble M. F., Rood H. J., 1999, *ApJS*, 125, 35
- Takizawa M., 2000, *ApJ*, 532,183
- Vijayaraghavan R., Ricker P. M., 2013, *MNRAS*, 435, 2713
- White D. A., Fabian A.C., 1995, *MNRAS*, 273, 72

This paper has been typeset from a $\text{\TeX}/\text{\LaTeX}$ file prepared by the author.

Table 7. List of member galaxies of Abell 3653. The galaxies numbered 19, 22, 28 and 71 are from 6dF survey.

#	Object Name	RA (J2000)	Dec (J2000)	Velocity km/s	Redshift	Magnitude Filter
1	GALEXASC J195249.91-520139.6	298.20825	-52.02811	31928	0.1065	17.5R
2	ABELL 3653:PRD 351	298.25292	-52.02064	32587	0.1087	17.7R
3	2MASX J19525707-5202462	298.23787	-52.04611	32887	0.1097	16.2R
4	2MASX J19530336-5202132	298.26404	-52.03700	32947	0.1099	11.2R
5	ABELL 3653:PRD 133	298.27417	-52.02500	32198	0.1074	18.4R
6	ABELL 3653:PRD 347	298.22688	-52.05733	32737	0.1092	17.4R
7	ABELL 3653:PRD 285	298.27729	-52.03906	32947	0.1099	18.1R
8	ABELL 3653:PRD 010	298.18763	-51.99322	31298	0.1044	17.2R
9	ABELL 3653:PRD 349	298.23954	-51.97142	31628	0.1055	17.9R
10	ABELL 3653:PRD 018	298.13488	-52.00225	32108	0.1071	18.1R
11	GALEXASC J195313.18-520313.3	298.30600	-52.05344	32617	0.1088	18.2R
12	ABELL 3653:PRD 050	298.16692	-52.07353	32977	0.1100	18.2R
13	ABELL 3653:PRD 101	298.12083	-52.02139	32258	0.1076	17.7R
14	ABELL 3653:PRD 035	298.10217	-52.04547	30549	0.1019	18.7R
15	GALEXASC J195239.36-520549.8	298.16367	-52.09700	31868	0.1063	17.7R
16	GALEXASC J195306.88-515647.9	298.27804	-51.94678	31478	0.1050	17.1R
17	ABELL 3653:PRD 338	298.12354	-52.08539	31868	0.1063	17.7R
18	ABELL 3653:PRD 245	298.08171	-52.02192	31598	0.1054	17.6R
19	2MASX J19521735-5159465	298.07238	-51.99622	32221	0.1075	16.1b
20	2MASX J19531237-5206322	298.30163	-52.10883	31178	0.1040	16.9R
21	ABELL 3653:PRD 230	298.06113	-52.00808	32198	0.1074	17.8R
22	2MASX J19521995-5205095	298.08312	-52.08589	31604	0.1054	15.9R
23	GALEXASC J195211.95-520042.3	298.04983	-52.01147	29769	0.0993	17.6R
24	ABELL 3653:PRD 029	298.04363	-52.00411	32348	0.1079	17.9R
25	ABELL 3653:PRD 006	298.31296	-51.92744	31298	0.1044	18.7R
26	ABELL 3653:PRD 358	298.38788	-51.97586	32468	0.1083	17.8R
27	GALEXASC J195308.09-515501.9	298.28367	-51.91731	32827	0.1095	18.0R
28	2MASX J19531839-5155491	298.32646	-51.93039	30836	0.1029	16.1R
29	GALEXASC J195209.58-520339.2	298.03967	-52.06108	31658	0.1056	17.3R
30	ABELL 3653:PRD 340	298.14100	-51.91719	32468	0.1083	18.1R
31	ABELL 3653:PRD 057	298.35767	-52.11078	30999	0.1034	17.9R
32	2MASX J19531914-5155201	298.3300	-51.92233	31298	0.1044	16.4R
33	ABELL 3653:PRD 334	298.04671	-51.96708	31178	0.1040	17.9R
34	GALEXASC J195336.19-515744.5	298.39996	-51.96253	30279	0.1010	17.9R
35	ABELL 3653:PRD 198	298.25192	-52.15142	31568	0.1053	18.8R
36	ABELL 3653:PRD 362	298.41796	-52.06881	33727	0.1125	17.8R
37	ABELL 3653:PRD 172	298.01963	-51.98944	31658	0.1056	18.0R
38	ABELL 3653:PRD 049	298.24442	-52.15547	31868	0.1063	18.3R
39	GALEXASC J195326.15-520801.2	298.35921	-52.13342	34386	0.1147	19.1R
40	2MASX J19531989-5154211	298.33308	-51.90594	32917	0.1098	17.0R
41	2MASX J19515849-5203084	297.99375	-52.05239	32767	0.1093	16.2R
42	ABELL 3653:PRD 332	297.99037	-52.00719	31418	0.1048	18.3R
43	ABELL 3653:PRD 007	298.37521	-51.91339	32917	0.1098	18.3R
44	ABELL 3653:PRD 282	298.44896	-52.07464	32737	0.1092	18.0R
45	ABELL 3653:PRD 130	298.39583	-52.13614	31718	0.1058	17.1R
46	ABELL 3653:PRD 364	298.42821	-52.11667	32138	0.1072	17.2R
47	GALEXASC J195304.51-515211.0	298.26929	-51.86925	31928	0.1065	17.4R
48	ABELL 3653:PRD 331	297.97608	-51.96444	32498	0.1084	17.7R
49	2MASX J19530945-5211122	298.28933	-52.18678	33187	0.1107	16.7R
50	ABELL 3653:PRD 090	298.01667	-51.91583	32587	0.1087	17.4R
51	GALEXASC J195254.41-515127.2	298.22683	-51.85711	30699	0.1024	18.5R
52	GALEXASC J195155.56-520639.7	297.98146	-52.11133	32647	0.1089	18.0R
53	ABELL 3653:PRD 279	298.49304	-52.06967	32677	0.1090	18.2R
54	2MASX J19535592-5205196	298.48292	-52.08881	31328	0.1045	16.4R
55	ABELL 3653:PRD 328	297.94571	-51.97167	32348	0.1079	18.4R
56	GALEXASC J195226.88-515104.1	298.11175	-51.85139	30729	0.1025	17.3R
57	ABELL 3653:PRD 093	297.96383	-51.92294	33397	0.1114	18.1R
58	GALEXASC J195139.34-520231.9	297.91392	-52.04194	32887	0.1097	17.2R
59	ABELL 3653:PRD 066	298.52496	-52.07533	33067	0.1103	17.7R
60	ABELL 3653:PRD 026	297.93000	-51.94375	32917	0.1098	17.6R

Table 7. continued.

#	Object Name	RA (J2000)	Dec (J2000)	Velocity km/s	Redshift	Magnitude Filter
61	GALEXASC J195341.68-515207.5	298.42367	-51.86858	33157	0.1106	18.2R
62	ABELL 3653:PRD 121	298.17492	-52.22450	32468	0.1083	18.8R
63	GALEXASC J195412.11-520133.6	298.55071	-52.02583	33157	0.1106	17.6R
64	2MASX J19513315-5202553	297.88796	-52.04878	32198	0.1074	16.9R
65	ABELL 3653:PRD 003	298.53050	-51.93383	30999	0.1034	18.2R
66	2MASX J19532263-5213301	298.34417	-52.22506	32587	0.1087	16.5R
67	GALEXASC J195301.00-514835.7	298.25417	-51.80981	33697	0.1124	17.6R
68	ABELL 3653:PRD 124	298.38650	-52.21856	32318	0.1078	18.5R
69	ABELL 3653:PRD 186	298.36450	-52.22814	32348	0.1079	18.2R
70	ABELL 3653:PRD 325	297.91596	-52.14275	32018	0.1068	18.4R
71	2MASX J19541986-5158230	298.58279	-51.97308	33162	0.1106	15.9R
72	2MASX J19542245-5200250	298.59346	-52.00694	30219	0.1008	16.6R
73	ABELL 3653:PRD 140	298.59604	-52.03164	33847	0.1129	18.1R
74	GALEXASC J195355.47-521137.6	298.48092	-52.19364	33847	0.1129	16.9R
75	ABELL 3653:PRD 031	297.84621	-52.04850	32258	0.1076	17.9R
76	ABELL 3653:PRD 120	298.11296	-52.25203	32108	0.1071	17.9R
77	GALEXASC J195253.38-514642.8	298.22225	-51.77856	31478	0.1050	19.4R
78	ABELL 3653:PRD 080	298.41883	-51.80536	32887	0.1097	17.4R
79	GALEXASC J195117.03-520619.7	297.81967	-52.10514	32378	0.1080	18.7R
80	2MASX J19532972-5216226	298.37396	-52.27300	32767	0.1093	17.0R
81	ABELL 3653:PRD 141	298.65158	-51.99289	31478	0.1050	18.2R
82	ABELL 3653:PRD 181	297.96808	-52.24167	31748	0.1059	18.6R
83	ABELL 3653:PRD 135	298.66808	-52.05789	32498	0.1084	18.0R
84	2MASX J19515019-5148042	297.95904	-51.80125	30609	0.1021	17.4R
85	2MASX J19543069-5209140	298.62792	-52.15383	31838	0.1062	16.5R
86	ABELL 3653:PRD 051	298.34125	-52.29897	32647	0.1089	17.8R
87	ABELL 3653:PRD 187	298.51992	-52.26153	31748	0.1059	18.9R